

1 **Adaptive covariance hybridization for the assimilation**  
2 **of SST observations within a coupled Earth system**  
3 **reanalysis**

4 **Sébastien Barthélémy<sup>1</sup>, François Counillon<sup>1,2</sup>, Yiguo Wang<sup>2</sup>**

5 <sup>1</sup>Geophysical Institute, University of Bergen and Bjerknes Centre for Climate research, Bergen, Norway

6 <sup>2</sup>Nansen Environmental and Remote Sensing Centre and Bjerknes Centre for Climate Research, Bergen,  
7 Norway

8 **Key Points:**

- 9 • Hybrid covariance handles sampling error and improves the update of deep wa-  
10 ter masses when assimilating surface observation with an EnKF  
11 • The method is well suited to provide a long coupled reanalysis of the past century  
12 • Hybrid covariance with adaptive hybrid coefficients explicitly estimated in space  
13 and time achieved the best performance

---

Corresponding author: Sébastien Barthélémy, [sebastien.barthelemy@uib.no](mailto:sebastien.barthelemy@uib.no)

**Abstract**

Ensemble data assimilation methods, such as the Ensemble Kalman Filter, are well suited for climate reanalysis and predictions because they feature flow-dependent covariance, and the ensemble can be used to estimate the uncertainty of the system. However, because Earth System Models are heavy computationally, the method typically uses a few tens of members. Sampling error in the covariance matrix can introduce biases in the unobserved regions (e.g. in the deep ocean), which may cause a drift in the reanalysis and in the predictions. Here, we assess the potential of the hybrid covariance approach (EnKF-OI) to counteract sampling error and rank deficiencies. The EnKF-OI linearly combines the superior flow-dependent covariance computed from a dynamical ensemble with another covariance matrix that is static but less prone to sampling error. We test the method within the Norwegian Climate Prediction Model (NorCPM), which combines the Norwegian Earth System Model (NorESM) and the Ensemble Kalman Filter (EnKF). We test the performance of the reanalyses in an idealised twin experiment, where we assimilate synthetic sea surface temperature observations monthly for the period 1980-2010. The dynamical ensemble consists of 30 members, and the static ensemble is composed of 315 seasonal members sampled from a long stable pre-industrial run. We compare the performance of the EnKF to 1) an EnKF-OI with a global hybrid coefficient tuned empirically, referred to as standard hybrid and 2) an EnKF-OI with adaptive hybrid coefficients explicitly estimated in space and time. Both hybrid covariance methods cure the bias introduced by the EnKF at intermediate and deep water. The adaptive EnKF-OI performs best overall, and that by doing smaller updates than the standard hybrid version. In the adaptive EnKF-OI, the hybrid coefficient remains nearly constant throughout the reanalysis, with only a weak seasonal variability.

**Plain Language Summary**

Data assimilation is a statistical method that reduces uncertainty in a model, based on observations. A popular method for climate reanalysis and prediction are ensemble method that relies on statistics from a finite ensemble of model realisations. However, observations are sparse – mostly near the surface – and the sampling error from data assimilation method introduces a degradation in the deep ocean. We use a method that complements this ensemble with a pre-existing database of model states to reduce sampling error. We show that the approach substantially reduces error at the intermediate and deep ocean. The method typically requires the tuning of a parameter, but we show that it can be estimated online, achieving the best performance.

**1 Introduction**

Data assimilation estimates the state of a model (called the analysis) that approaches the “unknown true state” of the system based on observations, a prior model estimate, and statistical information on their uncertainties. Data assimilation is applied sequentially/recursively to provide a reanalysis, which can also be used to understand the mechanisms of variability and initialise predictions. Data assimilation has been one of the key ingredients in the progress of numerical weather prediction (Bauer et al., 2015) and is now used in a wide range of geosciences applications (Carrassi et al., 2018), including climate prediction. The ensemble Kalman Filter (EnKF, Evensen, 2003), is an advanced data assimilation method that provides flow-dependent covariance – *i.e.*, that can evolve in time and space with a transient state or a regime shift – and the ensemble provides a quantification of the uncertainty of the system. These properties are well suited for climate reanalysis and predictions, and the method is becoming increasingly popular in that field (*e.g.*, Zhang et al., 2009; Counillon et al., 2014; Brune et al., 2015; Karspeck et al., 2018; O’Kane et al., 2019).

63 Ensemble-based data assimilation methods (e.g., the EnKF) approximate the fore-  
 64 cast error covariance matrix using a finite-size ensemble from a Monte Carlo integration  
 65 step. Rank deficiencies and sampling errors emerge and deteriorate the performance of  
 66 the system, causing an artificial reduction of the ensemble spread and may even lead to  
 67 filter divergence. Several ad-hoc methods have been introduced to counteract sampling  
 68 errors. Localization (Houtekamer & Mitchell, 2001; Evensen, 2003; Ott et al., 2004; An-  
 69 derson, 2007) limits the spatial extent of the corrections, based on the approximation  
 70 that the covariance function decays as a function of the distance – and can be seen as  
 71 a way to effectively reduce the degree of freedom of the system. Inflation (Anderson, 2001;  
 72 Whitaker & Hamill, 2012; Raanes et al., 2019) counteracts the spread-collapse by arti-  
 73 ficially inflating the ensemble spread at every assimilation step. The last method is the  
 74 covariance hybridization method, which is the topic of our paper.

75 Covariance hybridization (Hamill & Snyder, 2000) combines linearly the flow-dependent  
 76 covariance computed from a finite Monte-Carlo ensemble with another covariance ma-  
 77 trix that is less prone to sampling error. The static matrix can be parameterized (Hamill  
 78 & Snyder, 2000; Weaver & Courtier, 2001), computed from a long model simulation (Counillon  
 79 et al., 2009), computed as the average of the background error covariance matrices from  
 80 a previous data assimilation run (Carrió et al., 2021) or computed from a dynamical en-  
 81 semble at a lower resolution (Rainwater & Hunt, 2013). The hybrid covariance method  
 82 achieves better performance than the standalone EnKF, particularly for small ensem-  
 83 bles, and performance converges to that of the EnKF for large ensembles (X. Wang et  
 84 al., 2007; Counillon et al., 2009; Raboudi et al., 2019). The computational cost of the  
 85 hybrid covariance methods is customizable to the desired cost.

86 The linear coefficients combining the static and the dynamic covariance are called  
 87 the "hybridization coefficients", which optimally balances the superior but noisy sam-  
 88 ple covariance with that of less noisy but static covariance. To achieve optimal perfor-  
 89 mance, it is crucial to tune these coefficients (X. Wang et al., 2007; Counillon et al., 2009;  
 90 Raboudi et al., 2019; Gharamti et al., 2014). The optimal values of these coefficients de-  
 91 pend on the non-stationarity of the dynamical system as well as the data assimilation  
 92 settings, such as the dynamical ensemble size, localisation and inflation settings. As such,  
 93 it is expected that the optimal value of the hybridization coefficients should vary in space  
 94 and time. A first attempt to estimate spatial and time-varying hybridization coefficient  
 95 has been developed (Gharamti, 2020) with a Bayesian framework (using fixed localisa-  
 96 tion settings). They found that a spatially heterogeneous hybridization coefficient for-  
 97 mulation outperforms a homogeneous formulation. Ménétrier and Auligné (2015) and  
 98 Ménétrier et al. (2015) formulated the problem of hybridization as a linear filtering prob-  
 99 lem of the background error covariance matrix to optimize both the localization and the  
 100 hybridization coefficients simultaneously.

101 In this work, we aim to investigate the benefit of background error covariance hy-  
 102 bridization for climate reanalysis and climate prediction systems, as for example with  
 103 the CMIP6 Decadal Climate Prediction Project (DCPP, Boer et al., 2016). We use the  
 104 Norwegian Climate Prediction Model (NorCPM, Counillon et al., 2014, 2016) that pro-  
 105 vides coupled reanalysis and contributed to CMIP6 DCPP (Bethke et al., 2021). Here,  
 106 we focus on long coupled reanalysis as NorCPM will produce such a reanalysis from 1850  
 107 to the present. Sea surface temperature (SST) dominates the ocean observation network  
 108 before the emergence of altimetry in the 90s and Argo data in the 2000s. Using only SST,  
 109 NorCPM can control the upper ocean heat content, and major indices of climate vari-  
 110 ability in the North Atlantic well (Counillon et al., 2016). Two features of NorCPM, flow-  
 111 dependent assimilation and assimilation in isopycnal coordinates, were found to be par-  
 112 ticularly important in that success. However, it also yields an unrealistic update of the  
 113 intermediate water masses in the North Atlantic Subpolar Gyre (SPG) (typically below  
 114 1000 m) (Counillon et al., 2016), which subsequently causes a drift in the multi-year pre-

115 dictions in the North Atlantic SPG region (Bethke et al., 2018). We aim to address this  
116 limitation in our current assimilation system.

117 We test the performance of NorCPM for coupled reanalysis in the framework of ide-  
118 alised twin experiments with the assimilation of SST. We assess whether 1) hybrid co-  
119 variance can solve this issue and compare the performance of a 31-year coupled reanal-  
120 ysis produced with the EnKF (currently used in NorCPM) and hybrid covariance meth-  
121 ods; 2) compare robustness and optimality of two flavours of hybrid covariance meth-  
122 ods: one using an empirically tuned globally constant hybridization coefficient and one  
123 where the hybridization coefficients are estimated adaptively in space and time (Ménétrier  
124 et al., 2015; Ménétrier & Auligné, 2015; Ménétrier, 2021).

125 The results show that the hybridization method – both with fixed and adaptive hy-  
126 bridization coefficients – performs equally or better than the EnKF in most places and  
127 depths, and substantially improves results in intermediate and deep water masses. The  
128 adaptive hybrid performs better than its counterpart with fixed hybridization factors.

129 This paper is organised as follows. Section 2 presents the Earth System Model (ESM)  
130 used in this work, the Norwegian Earth System Model (NorESM). Section 3 presents the  
131 deterministic EnKF, and its practical implementation within the NorCPM. Section 4 de-  
132 scribes hybridization with a static covariance matrix. Section 5 describes the adaptive  
133 covariance hybridization method and its practical implementation within NorCPM for  
134 SST assimilation. In section 6, we introduce the experimental design and the evaluation  
135 metrics. The numerical results are presented in section 7. Section 8, provides a conclu-  
136 sion, discussion and future perspective to this work.

## 137 **2 Model system: the Norwegian Earth System Model**

138 NorESM1-ME (Bentsen et al., 2013) is based on version 1.0.4 of the Community Earth  
139 System Model (Hurrell et al., 2013). Its atmosphere component is the CAM4-OSLO, the  
140 ocean component is the Bergen Layered Ocean Model, BLOM, (Bentsen et al., 2013),  
141 the land component is the Community Land Model, CLM4, (Lawrence et al., 2011), the  
142 sea ice component is the Los Alamos Sea Ice Model, CICE4, (Bitz et al., 2012), and the  
143 coupler is CPL7 (Craig et al., 2012).

144 The atmosphere and the land components have  $1.9^\circ \times 2.5^\circ$  latitude-longitude res-  
145 olution. The atmosphere component has 26 hybrid sigma-pressure levels ranging from  
146 the surface up to 3 hPa. The ocean and the sea ice components have a  $1^\circ$  horizontal res-  
147 olution in both latitude and longitude with a bipolar grid. BLOM comprises in the ver-  
148 tical a stack of 51 isopycnic layers and two layers for representing the bulk mixed layer.  
149 Before 2005, the forcings are the CMIP5 historical forcings (Taylor et al., 2012), while  
150 after 2005, they are the representative Concentration Pathway 8.5 forcings (van Vuuren  
151 et al., 2011).

## 152 **3 The deterministic ensemble Kalman filter**

153 Let  $\mathbf{X} \in \mathbb{R}^{n \times N}$  an ensemble of  $N$  model states ( $\mathbf{x}_1, \mathbf{x}_2, \dots, \mathbf{x}_N$ ),  $\mathbf{x} \in \mathbb{R}^n$  the en-  
154 semble mean and  $\mathbf{A} \in \mathbb{R}^{n \times N}$  the ensemble anomalies. We note  $n$  the model state di-  
155 mension.  $\mathbf{x}$  and  $\mathbf{A}$  are given by Eq. (1) and (2):

$$156 \quad \mathbf{x} = \frac{1}{N} \mathbf{X} \mathbf{1}, \quad (1)$$

$$157 \quad \mathbf{A} = \mathbf{X} \left( \mathbf{I} - \frac{1}{N} \mathbf{1} \mathbf{1}^T \right), \quad (2)$$

158 where  $\mathbf{I} \in \mathbb{R}^{N \times N}$  is the identity matrix and  $\mathbf{1} \in \mathbb{R}^N$  is a vector with all elements equal  
 159 to 1. In the following equations, the superscripts f and a stand respectively for the fore-  
 160 casted and analysed states of the mean and the anomalies.

161 We note  $\mathbf{x}^t$  the true state of the system. The observations  $\mathbf{y}$  are defined by Eq. (3):

$$162 \quad \mathbf{y} = \mathbf{H}\mathbf{x}^t + \varepsilon, \quad \varepsilon \sim \mathcal{N}(\mathbf{0}, \mathbf{R}), \quad (3)$$

163 where  $\mathbf{H} \in \mathbb{H}^{p \times n}$  is the observation operator,  $\mathbf{R} \in \mathbb{R}^{p \times p}$  is the observation error co-  
 164 variance matrix, and  $p$  is the number of observations.

165 In this study, the deterministic EnKF (DEnKF) introduced by Sakov and Oke (2008)  
 166 is used. The DEnKF is a square-root (deterministic) flavour of the EnKF that solves the  
 167 analysis without the need for perturbation of the observations. It inflates the error by  
 168 construction and is intended to perform well in applications where corrections are small  
 169 (Sakov & Oke, 2008). The scheme has been robustly tested and validated (Sakov et al.,  
 170 2012; Counillon et al., 2016; Bethke et al., 2021). The DEnKF decomposes into two steps:  
 171 a forecast step and an analysis step. In the forecast step, each analyzed member  $\mathbf{x}_i^a$  is  
 172 integrated forward in time, which becomes the prior  $\mathbf{x}_i^f$  at the following assimilation cy-  
 173 cle:

$$174 \quad \mathbf{x}_i^f = \mathcal{M}(\mathbf{x}_i^a), \quad i = 1, \dots, N, \quad (4)$$

175 where  $\mathcal{M}$  is an operator that stands for the model integration.

176 The analysis step of the DEnKF proceeds in two steps, the update of the ensemble  
 177 mean, Eq. (5), and the update of the ensemble anomalies, Eq. (6):

$$178 \quad \mathbf{x}^a = \mathbf{x}^f + \mathbf{K}(\mathbf{y} - \mathbf{H}\mathbf{x}^f), \quad (5)$$

$$179 \quad \mathbf{A}^a = \mathbf{A}^f - \frac{1}{2}\mathbf{K}\mathbf{H}\mathbf{A}^f, \quad (6)$$

180 where:

$$181 \quad \mathbf{K} = \mathbf{P}^f \mathbf{H}^T \left( \mathbf{H} \mathbf{P}^f \mathbf{H}^T + \mathbf{R} \right)^{-1}, \quad (7)$$

$$182 \quad \mathbf{P}^f = \frac{\mathbf{A}^f \left( \mathbf{A}^f \right)^T}{N - 1}, \quad (8)$$

183 are respectively the Kalman gain matrix and the background error covariance matrix es-  
 184 timated from the ensemble anomalies.

185 In the following, the DEnKF will be referred to as EnKF since general conclusions  
 186 of this work are independent of the flavour of the EnKF analysis scheme used.

187 Applying an EnKF with a large dimensional system requires few ad-hoc implemen-  
 188 tations. In order to avoid a too abrupt start of assimilation, the variance of the obser-  
 189 vation error is multiplied by a factor 8 at the first assimilation cycle and is then reduced  
 190 by 1 every two months until it reaches 1 over the course of 14 months. We use the rfac-  
 191 tor inflation scheme (Sakov et al., 2012), for which the observation error is inflated by  
 192 2 when updating the ensemble anomaly in Eq. 6. We also use pre-screening of the ob-  
 193 servation; *i.e.*, the observation error variance is inflated so that the analysis remains within

194 2 standard deviations of the forecast error from the ensemble mean of the forecasts (Sakov  
 195 et al., 2012). We also used the upscaling method (Y. Wang et al., 2016) that handles the  
 196 update of the water layers thickness (truncated Gaussian) and better preserve mass, heat  
 197 and salt. For producing long reanalysis (from 1850) with SST assimilation, we use the  
 198 Hadley Centre Sea Ice and Sea Surface Temperature (HadISST2.1.0.0) available from  
 199 1850–present. This type of product is practical because it handles the biases between  
 200 different data set and provide a grided ensemble SST that can be used to quantify the  
 201 uncertainty. Still, it is constructed by statistical interpolation/extrapolation from the  
 202 raw data and the neighbouring observation errors are highly correlated. Our assimila-  
 203 tion code assumes the observation error to be independent (*i.e.*,  $\mathbf{R}$  is diagonal) and it  
 204 was therefore decided to only retain the nearest SST observation to update the water  
 205 column (we speak of "strong localization"). For more details about the implementation  
 206 of the EnKF within NorCPM, see Counillon et al. (2014) and Counillon et al. (2016).

#### 207 4 Background error covariance matrix hybridization

208 The dynamical covariance matrix  $\mathbf{P}_d^f$  is estimated from the dynamic ensemble  $\mathbf{X}_d$ .  
 209 The size of  $\mathbf{X}_d$  is limited to 30 members in the current version of NorCPM. Such a small  
 210 ensemble size results in spurious covariances (Anderson, 2007; Bishop & Hodyss, 2007)  
 211 and rank deficiencies (Oke et al., 2007). Background error covariance hybridization was  
 212 initially introduced by Hamill and Snyder (2000) to combine an EnKF with a 3DVar and  
 213 bring some flow-dependency in variational data assimilation. Covariance hybridization  
 214 has been used in sequential ensemble data assimilation by X. Wang et al. (2007), Counillon  
 215 et al. (2009) and Gharamti et al. (2014) (hereafter referred to as EnKF-OI) as a way to  
 216 limit the impact of under-sampling and rank deficiency. The background error covari-  
 217 ance matrix combines linearly a dynamical covariance matrix  $\mathbf{P}_d^f$  with another covari-  
 218 ance matrix  $\mathbf{P}_s^f$  (where the subscript  $s$  stands for static) computed from a climatolog-  
 219 ical ensemble of size  $N_s$ ,  $\mathbf{X}_s$  (where  $N_s \gg N_d$ ). That static ensemble is constructed by  
 220 gathering model output before running the assimilation experiment. As such, the EnKF-  
 221 OI does not increase the computational cost of the integration step and has only a lim-  
 222 ited impact on the computational cost of the analysis step (Counillon et al., 2009). In  
 223 the special case of the EnKF-OI in NorCPM the CPU-time of the EnKF-OI is 7% larger  
 224 than that of the standard EnKF; we discuss in Section 8 possible ways to reduce the com-  
 225 putational cost of the EnKF-OI in NorCPM. We denote  $\mathbf{P}_h^f$  the hybrid covariance ma-  
 226 trix:

$$227 \quad \mathbf{P}_h^f = \alpha_d \mathbf{P}_d^f + \alpha_s \mathbf{P}_s^f, \quad \alpha_d, \alpha_s \geq 0 \quad (9)$$

228 Unless explicitly mentioned, the sum of the coefficients  $\alpha_d$  and  $\alpha_s$  can be different  
 229 from 1.

230 The update of the mean and the anomalies with the EnKF-OI writes:

$$231 \quad \mathbf{x}_d^a = \mathbf{x}_d^f + \mathbf{K}_h (\mathbf{y} - \mathbf{H}\mathbf{x}_d^f), \quad (10)$$

$$232 \quad \mathbf{A}_d^a = \mathbf{A}_d^f - \frac{1}{2} \mathbf{K}_h \mathbf{H} \mathbf{A}_d^f, \quad (11)$$

233 where  $\mathbf{K}_h$  is the hybrid Kalman gain,

$$234 \quad \mathbf{K}_h = \mathbf{P}_h^f \mathbf{H}^T \left( \mathbf{H} \mathbf{P}_h^f \mathbf{H}^T + \mathbf{R} \right)^{-1}. \quad (12)$$

235 In practice, we do not compute explicitly the hybrid covariance matrix  $\mathbf{P}_h$ :

$$\mathbf{P}_h = \frac{\mathbf{A}_h (\mathbf{A}_h)^T}{N_h - 1}, \quad (13)$$

where  $\mathbf{A}_h$  stands for the hybrid anomalies (Counillon et al., 2009):

$$\mathbf{A}_h = \sqrt{N_h - 1} \left[ \sqrt{\frac{\alpha_d}{N_d - 1}} \mathbf{A}_d, \sqrt{\frac{\alpha_s}{N_s - 1}} \mathbf{A}_s \right], \quad (14)$$

and  $[\cdot, \cdot]$  stand for the concatenation of two sets of vectors. Therefore, the EnKF-OI is implemented within NorCPM following Evensen (2003) and Sakov et al. (2010).

## 5 Adaptive covariance hybridization

### 5.1 Explicit optimality of the hybridization coefficients

In this section, we build on the work of Ménétrier et al. (2015); Ménétrier and Auligné (2015) and adapt a method proposed in Ménétrier (2021) to determine the optimal hybridization coefficients.

We take advantage of the strong localization setting (see Section 3) to consider only the covariance between a single point at the surface of the ocean, and the multivariate state vector of the water column below so that the covariance matrix in each point reduces to a vector. In the following, we note  $\mathbf{P}$  the true covariance vector at a given point (which would be obtained with an infinite ensemble). We use the subscript  $i$  to refer to the  $i^{\text{th}}$  element of the covariance vector (*e.g.*,  $\mathbf{P}_i$  for the  $i^{\text{th}}$  element of the true covariance vector). We define the scalar product of two random vectors  $X$  and  $Y$  as  $\mathbb{E}[X \cdot Y] = \sum_{i=1}^p \mathbb{E}[X_i Y_i]$ . We assume that  $\mathbf{P}_d$  and  $\mathbf{P}$  are realizations of two independent random processes and that the sampling error of  $\mathbf{P}_d$ , *i.e.*,  $\mathbf{P}_d - \mathbf{P}$ , is unbiased, and orthogonal to the truth, (see Ménétrier et al. (2015), Eqs. (20a)-(20b)). Therefore:

$$\mathbb{E}[\mathbf{P}_d - \mathbf{P}] = 0, \quad (15a)$$

$$\mathbb{E}[(\mathbf{P}_d - \mathbf{P}) \cdot \mathbf{P}] = 0. \quad (15b)$$

The optimal hybridization coefficients  $(\alpha_d, \alpha_s)$  are defined as those minimizing, in a statistical sense, the square of the error between  $\mathbf{P}_h$  and  $\mathbf{P}$ , *i.e.*,  $(\alpha_d, \alpha_s)$  minimize the function  $e$ :

$$e(\alpha_d, \alpha_s) = \mathbb{E}[\|\mathbf{P}_h - \mathbf{P}\|^2] = \mathbb{E}[\|\alpha_d \mathbf{P}_d + \alpha_s \mathbf{P}_s - \mathbf{P}\|^2], \quad (16)$$

where  $\|\cdot\|$  stands for the  $L_2$ -norm of a vector. It can be shown (see Appendix A) that minimizing the function  $e$  is equivalent to solving a system of two equations, with unknown  $\alpha_d$  and  $\alpha_s$ , whose solution is given by:

$$(\alpha_d, \alpha_s) = \left( \frac{n_d}{\Delta}, \frac{n_s}{\Delta} \right), \quad (17)$$

where:

$$\Delta = \|\mathbf{P}_s\|^2 \mathbb{E}[\|\mathbf{P}_d\|^2] - \mathbb{E}[\mathbf{P}_d \cdot \mathbf{P}_s]^2, \quad (18)$$

$$n_d = \|\mathbf{P}_s\|^2 \mathbb{E}[\|\mathbf{P}\|^2] - \mathbb{E}[\mathbf{P}_d \cdot \mathbf{P}_s]^2, \quad (19)$$

$$n_s = \left( \mathbb{E}[\|\mathbf{P}_d\|^2] - \mathbb{E}[\|\mathbf{P}\|^2] \right) \mathbb{E}[\mathbf{P}_d \cdot \mathbf{P}_s]. \quad (20)$$

270 **5.2 Properties**

271 The properties highlighted by Ménétrier et al. (2015) in the case of the dual optimiza-  
 272 tion of localization and hybridization hold here:

- 273 1. **Behavior of the hybridization coefficients:** if the static covariance is mul-  
 274 tiplied by a factor  $\lambda$ , then  $\alpha_s$  is divided by  $\lambda$ , while  $\alpha_d$  remains unchanged. As such,  
 275 it is not necessary to tune the static covariance with a scalar a priori, as done in  
 276 Evensen (2003), Oke et al. (2008) and Counillon et al. (2009).  
 277 2. **Asymptotic behavior:** with an infinite ensemble,  $\mathbb{E} [\|\mathbf{P}_d\|^2] = \mathbb{E} [\|\mathbf{P}\|^2]$ . We  
 278 can replace  $\mathbb{E} [\|\mathbf{P}_d\|^2]$  by  $\mathbb{E} [\|\mathbf{P}\|^2]$  in Eqs. (19)-(20), and obtain  $(\alpha_d, \alpha_s) = (1, 0)$   
 279 as expected – there is no need for hybridization.  
 280 3. **Benefits of hybridization:** whatever the choice of the static covariance (see Ap-  
 281 pendix B),

$$282 e(1, 0) \geq e(\alpha_d, \alpha_s), \tag{21}$$

283 showing the superiority of the hybrid scheme over the standalone EnKF.

- 284 4. **Optimality condition:** we can show that  $\mathbf{P}_h$  verifies the following optimality  
 285 condition:

$$286 \begin{cases} \frac{\partial e}{\partial \alpha_d} = 0 \\ \frac{\partial e}{\partial \alpha_s} = 0 \end{cases} \Leftrightarrow \mathbb{E} [(\mathbf{P}_d - \mathbf{P}_s) \cdot (\mathbf{P}_h - \mathbf{P})] = 0. \tag{22}$$

287 This means from a statistical point of view that  $\mathbf{P}_h$  is the orthogonal projection  
 288 of the true covariance  $\mathbf{P}$  onto a sub-space defined as  $\mathbf{P}_d + \mu (\mathbf{P}_s - \mathbf{P}_d)$  where  $\mu \in$   
 289  $\mathbb{R}$ , see Fig. 1.

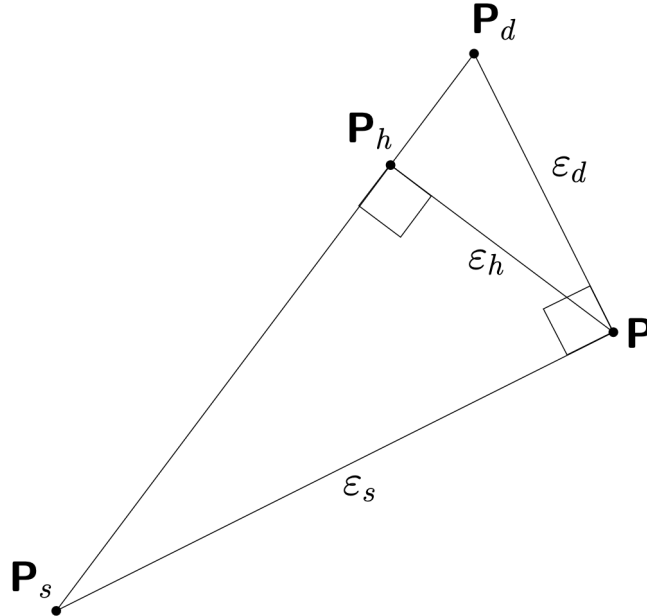


**Figure 1.** Geometrical representation of the orthogonal projection of the true covariance  $\mathbf{P}$  onto the sub-space generated by the dynamic covariance  $\mathbf{P}_d$  and the static covariance  $\mathbf{P}_s$ .

290 Here are some remarks:

- 291 1. if  $\alpha_d \neq 1$ ,  $\mathbf{P}_h$  can be interpreted as the linear interpolation between  $\mathbf{P}_d$  and  $\lambda\mathbf{P}_s$ ,  
 292 where:

$$293 \lambda = \frac{\alpha_s}{1 - \alpha_d}, \quad (23)$$

294 thus,  $\lambda \geq 1$  (resp  $\leq 1$ ) is equivalent to  $\alpha_d + \alpha_s \geq 1$  (resp.  $\leq 1$ ).  $\lambda$  acts as an in-  
 295 flation or deflation term for the matrix  $\mathbf{P}_s$  and  $\mathbf{P}_h$  is the linear interpolation be-  
 296 tween  $\mathbf{P}_d$  and the inflated/deflated  $\mathbf{P}_s$ .

- 297 2. From Eqs (15a)-(15b), it follows that the errors  $\mathbf{P}_d - \mathbf{P}$  and  $\mathbf{P}_s - \mathbf{P}$  are uncorre-  
 298 lated:  $\mathbb{E}[(\mathbf{P}_d - \mathbf{P}) \cdot (\mathbf{P}_s - \mathbf{P})] = 0$ . As a consequence, the triplet  $(\mathbf{P}_d, \mathbf{P}, \mathbf{P}_s)$  forms  
 299 a triangle rectangle in  $\mathbf{P}$ , see Fig. 1.  
 300 3. The numerator of  $\alpha_d$ ,  $n_d$ , can be interpreted as a measure of the collinearity of  
 301 the static covariance  $\mathbf{P}_s$ , and the expectation of the true covariance  $\mathbf{P}$ . Hence,  $n_d$   
 302 is equal to 0 if and only if  $\text{Var}(\mathbf{P}) = 0$  and  $\mathbf{P}$  and  $\mathbf{P}_s$  are collinear (or linearly de-  
 303 pendent). Conversely, if  $\mathbb{E}[\mathbf{P}_d \cdot \mathbf{P}_s] = 0$ , then  $\mathbf{P}$  and  $\mathbf{P}_s$  are orthogonal (see Ap-  
 304 pendix C).  
 305 4. It follows from Eq. (15b) that (see Appendix B, Eqs. (B1)-(B2)):

$$306 \mathbb{E}[\|\mathbf{P}_d - \mathbf{P}\|^2] = \mathbb{E}[\|\mathbf{P}_d\|^2] - \mathbb{E}[\|\mathbf{P}\|^2] \geq 0. \quad (24)$$

307 Therefore, the difference  $\mathbb{E}[\|\mathbf{P}_d\|^2] - \mathbb{E}[\|\mathbf{P}\|^2]$  can be interpreted as a measure  
 308 of the optimality (or the non-optimality) of the covariance function computed from  
 309 the dynamic ensemble  $\mathbf{P}_d$ : the smaller the difference, the smaller the distance  $\|\mathbf{P}_d - \mathbf{P}\|$   
 310 in a statistical sense. Conversely, the larger the difference, the larger the distance  
 311  $\|\mathbf{P}_d - \mathbf{P}\|$ .

- 312 5. It follows from remarks 3 and 4 that the hybridization coefficients  $\alpha_d$  and  $\alpha_s$  are  
 313 the combination of the optimality of the dynamic covariance function  $\mathbf{P}_d$  and the  
 314 collinearity/orthogonality of the static covariance  $\mathbf{P}_s$  and the true covariance  $\mathbf{P}$ .  
 315 6. As a consequence of Eq.(24) and Appendix C,  $0 \leq \alpha_d \leq 1$ . We can not give sim-  
 316 ilar upper and lower boundaries for the values of  $\alpha_s$ , as the term  $\mathbb{E}[\mathbf{P}_d \cdot \mathbf{P}_s]$  can  
 317 be negative and we do not know its lower bound. Numerical simulations showed  
 318 that this term is almost always positive (not shown). We can just say that  $\alpha_s$  is  
 319 maximal when  $\Delta$  is minimal and therefore  $\mathbb{E}[\mathbf{P}_d \cdot \mathbf{P}_s]$  is maximal. In that case,  
 320  $\alpha_d$  is minimal.

### 321 5.3 Practical implementation

322 Quantities in Eq. (19) and Eq. (20) can not be computed directly as they are a function  
 323 of  $\mathbb{E}[\|\mathbf{P}\|^2]$ ,  $\mathbb{E}[\mathbf{P}_d \cdot \mathbf{P}_s]$ , and  $\mathbb{E}[\|\mathbf{P}_d\|^2]$  that are unknown.

324 Nonetheless, the sampling theory developed in Ménétrier (2021) allows us to express  
 325  $\mathbb{E}[\mathbf{P}_i^2]$ ,  $i = 1, \dots, p$  as a function of the covariance and variance of the dynamic ensem-  
 326 ble. Using Eq. (101b) of Ménétrier (2021) one can write:

$$327 \mathbb{E}[\mathbf{P}_i^2] = \frac{(N_d - 1)^2}{(N_d - 2)(N_d + 1)} \mathbb{E}[\mathbf{P}_{di}^2] - \frac{N_d - 1}{(N_d - 2)(N_d + 1)} \mathbb{E}[\mathbf{v}_{di}\mathbf{v}_{d1}], \quad (25)$$

328 where  $\mathbf{v}_{di}$  is the variance of the dynamic ensemble for the  $i$ -th element of the model state.  
 329 The quantities  $n_d$ ,  $n_s$ , and  $\Delta$  are then fully expressed as a function of the static covari-  
 330 ance and the expectation of the variance and covariance of the dynamic ensemble.

331 The expectation terms in Eq. (18), (19), (20), and (25) are estimated under a sim-  
 332 plifying assumption of "local homogeneity": it is assumed that in an area surrounding  
 333 the water column, the vertical covariance functions are representative of the covariance  
 334 function of the water column. The expectation terms are then estimated as the average

335 of the surrounding vertical covariance functions. Numerical tests have shown that at least  
 336 500 covariance functions are necessary to compute reliable statistics. In this work, we  
 337 consider covariance functions in a radius up to 1000 km around the water column, which  
 338 usually provides between 500 and 1000 covariance functions to compute the expectation  
 339 terms.

340 In order to limit the computational burden of estimating the hybridization coeffi-  
 341 cients, they are computed on a subgrid of the domain (every 5 grid cells). The hybridiza-  
 342 tion coefficients are then interpolated to the remaining wet points using linear interpo-  
 343 lation of the neighbouring wet points.

344 The hybridization coefficients are estimated based on both temperature and salin-  
 345 ity. Doing so yields a lower root mean square error than when computing the hybridiza-  
 346 tion coefficients solely based on the temperature (not shown).

## 347 6 Experimental design and evaluation metrics

### 348 6.1 Experimental design

349 The free ensemble run (hereafter referred to as FREE), consists of 30 members run  
 350 with transient forcing from 1850 to 2014. The true run (hereafter referred to as TRUE)  
 351 is created by spawning one member (adding noise to surface temperature) on member  
 352 1 of FREE in 1960 and running it up to 2010. It was verified in Y. Wang et al. (2022)  
 353 that TRUE and member 1 of FREE were fully de-synchronised at the start of the ex-  
 354 periment in 1980. The synthetic observations of SST are generated by adding white noise  
 355 to the monthly SST of TRUE. The amplitude of the noise is set equal to the observa-  
 356 tion uncertainty (in space and time) of HadISST2. As in the real framework for assim-  
 357 ilation of SST, we do not use SST data under sea ice.

358 We produce reanalyses with monthly assimilation of SST observations from January  
 359 1980 to December 2010. All experiments start with the same initial dynamic ensemble  
 360 (taken from FREE in January 1980). The static ensemble is made from the monthly restarts  
 361 of a 315 years long stable pre-industrial run (monthly varying static ensemble). The ex-  
 362 periments are separated into three categories:

- 363 • **EnKF:** the standard EnKF used in NorCPM (Counillon et al., 2016).
- 364 • **Standard hybrid:** a constant and global hybridization coefficients (see Section  
 365 4). The sum of  $\alpha_d$  and  $\alpha_s$  is 1. We performed 7 reanalyses with  $\alpha_d = 0, 0.2, 0.4, 0.6, 0.8, 0.9, 1$ .  
 366 The case where  $\alpha_d = 0$  is equivalent to an ensemble of EnOI, and the case where  
 367  $\alpha_d = 1$  is equivalent to the standard EnKF.
- 368 • **Adaptive hybrid:** the hybridization coefficients are estimated at each assim-  
 369 ilation cycle, they vary spatially and their sum is not imposed equal to 1 (see Sec-  
 370 tion 5).

### 371 6.2 Evaluation metrics

372 The accuracy of the reanalyses is estimated based on the root mean square error (RMSE).  
 373 The RMSE is computed as:

$$374 \text{RMSE} = \sqrt{\sum_{i=1}^N \omega_i (\mathbf{x}_i - \mathbf{x}_i^t)^2}. \quad (26)$$

375 In the following, the RMSE is computed either over a time series at a given point  
 376 (in which case  $\omega_i = \frac{1}{N}$ ), or over the whole domain at a given time (in which case  $\omega_i$   
 377 is the relative size of the grid cell).

378 In order to easily compare RMSE between the nine different schemes (see Section 6.1),  
 379 we introduce the Mean Skill Score of one configuration  $i$ ,  $MSS_i$ . It is the relative reduction  
 380 of RMSE compared to the mean of the RMSE of the nine configurations, Eq. (27):

$$381 \quad MSS_i = 1 - \frac{RMSE_i}{\frac{1}{9} \sum_{j=1}^9 RMSE_j}, \quad (27)$$

382 where  $RMSE_i$  is the RMSE of one of the schemes. The MSS is 1 if the scheme is perfect  
 383 (RMSE is equal to 0), between 0 and 1 if the scheme performs better than the mean  
 384 of the other schemes and negative otherwise.

385 Another important metric to evaluate the relative efficiency of different data assimilation  
 386 schemes is to consider the “degrees of freedom for signal” (DFS, Cardinali et al.,  
 387 2004; Wahba et al., 1995). It can be interpreted as the number of modes of variability  
 388 reduced from the ensemble by the assimilation (*i.e.* the assimilation change). The DFS  
 389 is defined as follows:

$$390 \quad DFS = \frac{\partial \mathbf{H} \mathbf{x}_d^a}{\partial \mathbf{y}} = \text{Tr}(\mathbf{KH}) \quad (28)$$

391 The DFS is between 0 (*i.e.*, the observations have no impact on the ensemble), and  
 392 the total number of degrees of freedom (*i.e.*, observations has collapsed the number of  
 393 modes of variability into a single one, Xie et al., 2018). The total number of degrees of  
 394 freedom is the minimum between the ensemble size and the number of observations used  
 395 for the local assimilation. In NorCPM, in the context of strong localisation (where we  
 396 retain only the nearest observation, see Section 3), it implies that the DFS is between  
 397 0 and 1 (independently of the ensemble size). This allows for an inter-comparison of the  
 398 DFS even though the schemes have different ensemble sizes.

## 399 7 Results

### 400 7.1 Stability of the adaptive covariance hybridization

401 The adaptive covariance hybridization method (see Section 5) estimates adaptive hy-  
 402 bridization coefficients both in space and time.

403 Figure 2 shows the time series of globally averaged  $\alpha_d$ ,  $\alpha_s$ , and  $\alpha_d + \alpha_s$  (sea ice-covered  
 404 points where there are no SST data are masked). After a spin-up period of approximately  
 405 three years, the averaged values of the hybridization coefficients converge to a global av-  
 406 erage of 0.7 for  $\alpha_d$ , and 0.175 for  $\alpha_s$ . This shows that the mean values of  $\alpha_d$  and  $\alpha_s$   
 407 are stable in time and display a limited temporal variability despite an important spatial vari-  
 408 ability, and so does the sum  $\alpha_d + \alpha_s$ . Hence, the mean values of  $\alpha_d$  and  $\alpha_s$  computed  
 409 in specific basins show similar behaviour and converge within 3 years (not shown). The  
 410 global averaged value of  $\alpha_d + \alpha_s$  is roughly 0.875. Following remark 1 in Section 5.2,  
 411 it implies that the static ensemble has a larger error variance than the error growth within  
 412 one assimilation cycle and needs to be reduced - in agreement with Oke et al. (2008),  
 413 Counillon and Bertino (2009), and Evensen (2003).

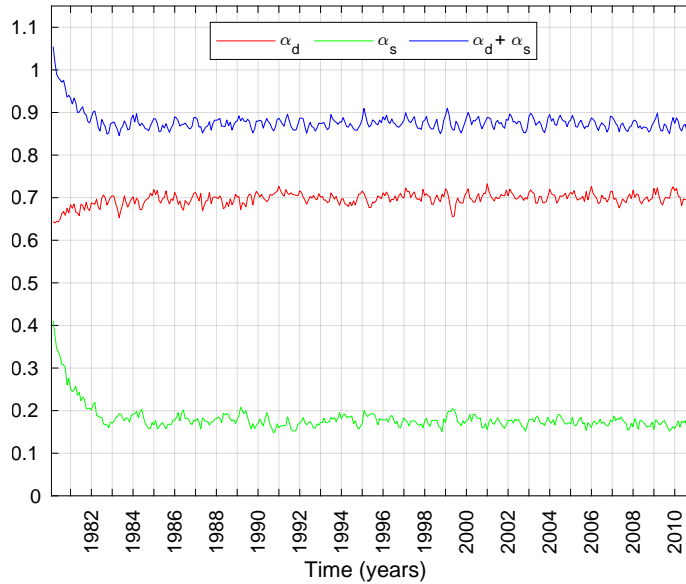


**Figure 2.** Time series of the global average values of  $\alpha_d$ ,  $\alpha_s$ , and  $\alpha_d + \alpha_s$ . Ice-covered regions are masked.

414 Figures 3 shows the pointwise averaged map of  $\alpha_d$  and  $\alpha_s$  computed over the years  
 415 1983 to 2010 for January and July. The values of  $\alpha_d$  display an important spatial vari-  
 416 ability with values ranging approximately from 0.4 up to 1. Regions where  $\alpha_d$  is small  
 417 coincide with places where  $\alpha_s$  is large. The spatial variations of the values of  $\alpha_d$  and  $\alpha_s$   
 418 (Section 5.2) can be explained from the perspective of the optimality of the dynamic covar-  
 419 iance  $\mathbf{P}_d$  (depending on the sampling error in the dynamical ensemble), and the collinear-  
 420 ity between the static covariance  $\mathbf{P}_s$  and the true covariance  $\mathbf{P}$  (meaning that static covar-  
 421 iance is sufficient). Larger values of  $\alpha_d$  are found in locations where the dynamic is  
 422 non-stationary and internal variability is large; *e.g.*, in the Northern part of the Atlantic  
 423 Ocean (Gulf Stream pathway, Subpolar Gyre, near the ice edge), the North Pacific, El  
 424 Niño–Southern Oscillation and in the Southern Ocean. Conversely, there are relatively  
 425 low values of  $\alpha_d$  in the Indian Ocean where variability is primarily externally forced (Guemas  
 426 et al., 2013), the decadal fluctuations are less pronounced than in the Atlantic or the Pa-  
 427 cific Ocean and where the Pacific Ocean teleconnections dominate the regionally driven  
 428 variability (Frankcombe et al., 2015). In the tropical Atlantic, the model is performing  
 429 very poorly and has no skill (Counillon et al., 2021); it is thus not surprising that  $\alpha_d$  is  
 430 also low.

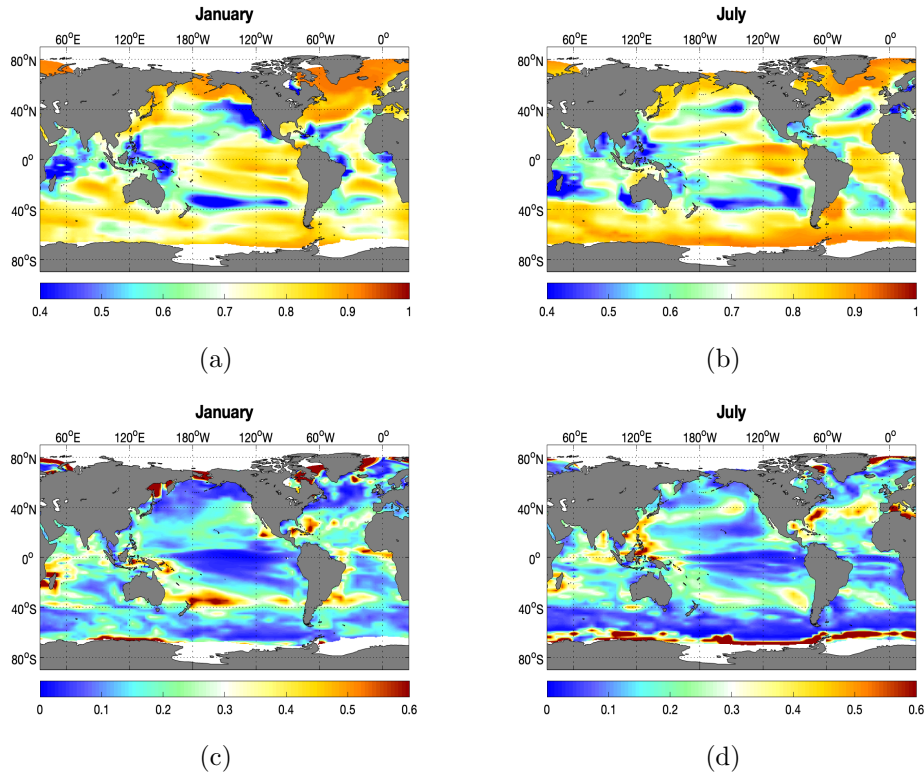


**Figure 3.** Pointwise averaged estimate of  $\alpha_d$  (top row), and of  $\alpha_s$  (bottom row) computed over 1983–2010 for the months of January and July.

431 In Fig. 4, we analyse the interannual de-seasoned standard deviation of the hybrid  
 432 coefficient beyond year 3 (once it has converged). We can see that the variability is very  
 433 small, except in a few places, *e.g.* in the Arctic, in Indian Ocean and in the tropical At-  
 434 lantic and Pacific Gyre. In those places, the performance between the standard hybrid  
 435 coefficient method is relatively small (not shown).

## 436 7.2 Intercomparison of the performance of the EnKF and the hybrid co- 437 variance schemes

438 Figure 5 shows the MSS (see Section 6.2) of ocean heat and salt content for the dif-  
 439 ferent schemes at different depth ranges (0–200 m, 200–500 m, ..., 2000–4000 m). We in-  
 440 clude the EnKF ( $\alpha_d = 1$  and  $\alpha_s = 0$ ) and the ensemble of EnOI ( $\alpha_d = 0$  and  $\alpha_s = 1$ )  
 441 as particular cases of the standard hybrid covariance method. A red cell (resp. blue cell)  
 442 indicates that the scheme provides a reduction (resp. an increase) of RMSE compared  
 443 to the average performance of all the schemes for a given depth range. For example, the  
 444 adaptive hybrid and the standard hybrid scheme with  $\alpha_d = 0.9$  reduces the RMSE of  
 445 the temperature at depth 500–1000 m by 10% compared to the average performance, while  
 446 the standard hybrid with  $\alpha_d = 0$  increases the RMSE at the depth 200–500 m by 15%.  
 447 The results for heat and salt content are very similar. As expected, the EnKF is out-  
 448 performing the ensemble of EnOI (*i.e.*,  $\alpha_d = 0$ ), showing the superiority of flow-dependent  
 449 covariance over static covariance. It also shows the importance of tuning the hybrid co-  
 450 efficient as for a large span of standard hybrid coefficient values, the hybrid covariance  
 451 methods perform poorer than the EnKF. When  $\alpha_d$  is larger than 0.8 ( $\alpha_d = 0.9$  being  
 452 optimal), the standard hybrid covariance outperforms the EnKF; notably between 2000  
 453 and 4000 m. In the latter, a bias is gradually increasing due to spurious covariance at

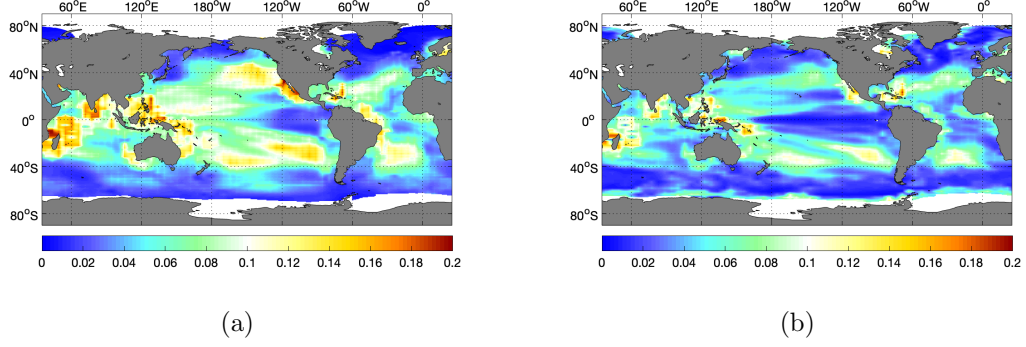


**Figure 4.** Standard-deviation of the de-seasoned values of  $\alpha_d$  (a), and of  $\alpha_s$  (b) computed over 1983–2010.

454 depth (Y. Wang et al., 2022; Bethke et al., 2018). The adaptive hybrid covariance method  
 455 performs best at nearly all depth levels for heat and salt content. In the following, we  
 456 will therefore present the adaptive hybrid and assess the spatial distribution of the im-  
 457 provements over the EnKF, but results with the best standard hybrid are nearly com-  
 458 parable (not shown).

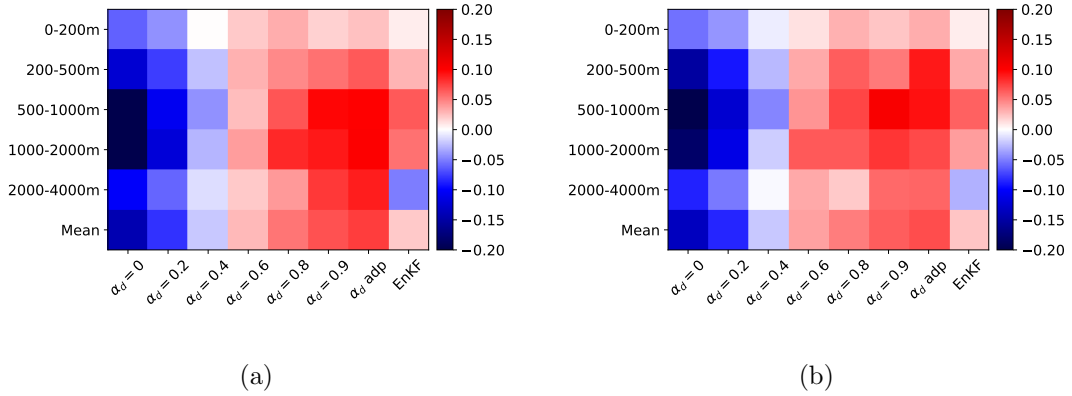


**Figure 5.** MSS of all the schemes for temperature (a) and salinity (b) at different depth intervals.  $\alpha_d = 0, \alpha_d = 0.2, \dots, \alpha_d = 0.9$  refer to the hybridization coefficient of the standard hybrid.  $\alpha_d = 0$  is the ensemble of EnOI, full static case, and  $\alpha_d = 1$  is the EnKF – the default scheme used in NorCPM. "α adp" stands for the adaptive hybridization scheme. The warm colour indicates that the scheme performs better than the average skill of all systems.

459 The adaptive hybrid and the EnKF achieve similar performance in the top 1000 m  
 460 (Figure 5), and we focus on performance below this depth range. We compare the re-  
 461 duction of RMSE of the EnKF and the adaptive hybrid compared to that of FREE for  
 462 two depths range.

463 Between 1000 and 2000 m (Fig. 6), the EnKF reduces the error overall (warmer value  
 464 is predominant) compared to FREE. Still, there are few places where it increases the RMSE  
 465 of temperature, *e.g.*: in the North Pacific, the subtropical Atlantic, and near the Wed-  
 466 dell Sea. Results are relatively comparable for salt content (see Fig. 6-b). The overall  
 467 pattern is similar with the adaptive hybrid. Still, it yields further improvement, as in  
 468 the North Atlantic subpolar gyre and it mitigates the degradation in the aforementioned  
 469 regions. The degradation in the Weddell Sea is nearly completely removed.

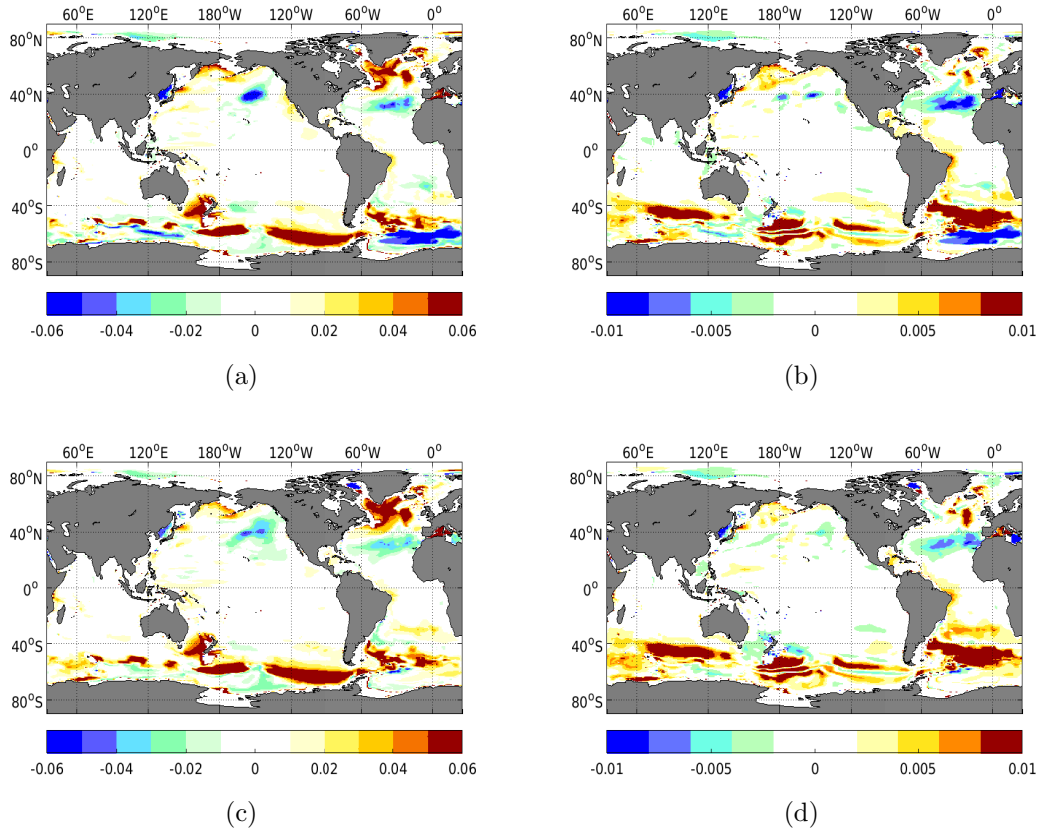


**Figure 6.** RMSE difference between FREE and the EnKF (a,b), and FREE and the adaptive hybrid (c,d) between 1000 and 2000 m depth for the temperature (left column) and the salinity (right column). Warm colour indicates that assimilation reduces error compared to FREE.

470 Between 2000 and 4000 m (Fig. 7), the EnKF degrades overall performance compared to  
 471 FREE. The degradation is larger in the North Pacific, the North Atlantic, and the  
 472 Southern Ocean for both the temperature and the salinity. The improvements are also  
 473 limited to the South Atlantic Ocean. The adaptive hybrid corrects or mitigates these bi-  
 474 ases. Some degradation remains (in the North Atlantic subpolar gyre, the Sea of Japan  
 475 in particular for salinity), but the assimilation yields an overall improvement over FREE.

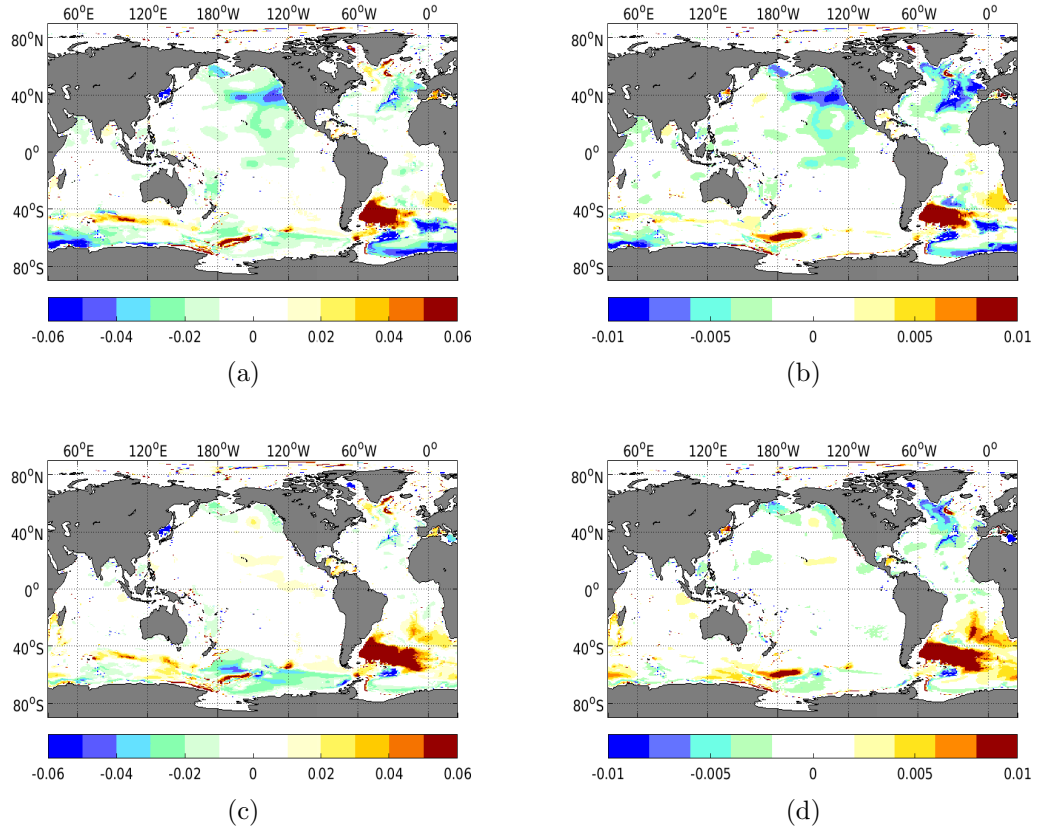


**Figure 7.** Same as fig. 6 but for 2000–4000 m depth interval.

476 An ideal assimilation system achieves minimal error while making the smallest change  
 477 possible during the assimilation. Figure 8 shows the difference of DFS (that quantifies  
 478 the assimilation change) between the EnKF and the best standard hybrid ( $\alpha_d = 0.9$ )  
 479 (panel a) and between the EnKF and the adaptive hybrid (panel b). The standard hy-  
 480 brid has a larger DFS value than the EnKF (negative values), implying that the data  
 481 assimilation induces more change. This is most notable in the Southern Ocean and the  
 482 tropical Pacific. In the Southern Ocean, the standard hybrid covariance method performs  
 483 better than the EnKF, so it can be argued that the larger corrections are beneficial. How-  
 484 ever, in the tropical Pacific, the  $\Delta\text{RMSE}$  of the two remains quite close, meaning the anal-  
 485 ysis induces more changes without improving performance. On the contrary, the adap-  
 486 tive hybrid, Fig. 8-(b), has a DFS close to that of the EnKF. There are some slight dif-  
 487 ferences (in the North Pacific, the North Atlantic, and the Southern Ocean), with a max-  
 488 imum in the Irminger Sea, where it strongly outperforms the EnKF (*e.g.*, 1000–2000 m).  
 489 It implies that the adaptive hybrid induces only change where this yields improved per-  
 490 formance.

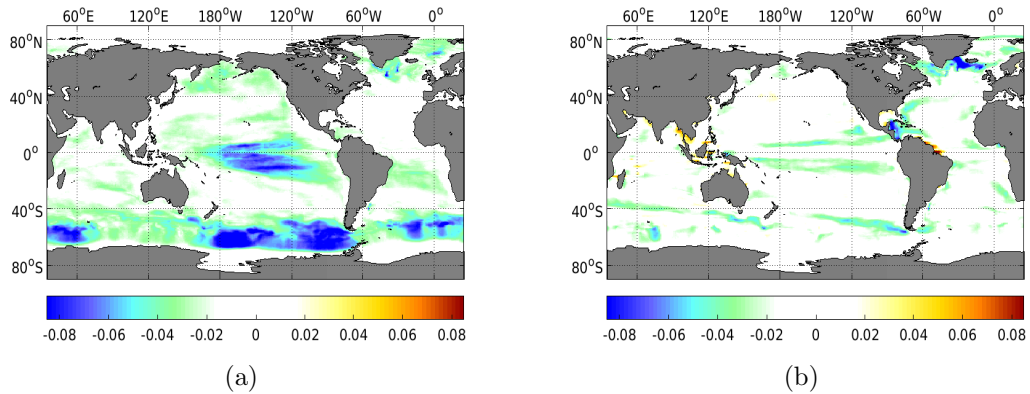


**Figure 8.** Difference of DFS between the EnKF and the standard hybrid covariance with  $\alpha_d = 0.9$  (a), and between EnKF and adaptive hybrid covariance (b). The cold colour indicates that the hybrid covariance yields a larger reduction of DFS than with the EnKF.

## 8 Discussion and conclusion

In this work, we compare two different versions of hybrid covariance data assimilation with the standard EnKF for producing climate reanalysis. We use the Norwegian Climate Prediction Model (NorCPM) and work in an idealised twin experiment framework. The reanalyses are performed with sole assimilation of SST for the period 1980-2010. In the first hybrid coefficient method, the hybridization coefficients are tuned empirically to optimize the performance, while in the second, the hybridization coefficients are estimated adaptively, both in space and time. The two hybrid coefficient methods outperform the standard EnKF and mitigate the degradation it introduces in the intermediate and deep ocean compared to unassimilated simulations. The adaptive performs best and is doing so by making smaller corrections than the standard hybrid. The hybridization coefficients with the adaptive hybrid are converging quickly (less than 3 years) to stable values and only show small seasonal variations.

Other alternatives have been developed in parallel to address the sampling error with the EnKF in NorCPM – namely the isopycnal vertical localization (Y. Wang et al., 2022). The latter limits the assimilation update of temperature and salinity to a fixed isopycnal level and was shown to mitigate the degradation seen in the standard EnKF. Combining the two approaches is straightforward and will be tested in the future. However, the isopycnal vertical localization detailed in Y. Wang et al. (2022) was tuned for an ensemble size of 30 members, while now the ensemble size is much larger (350 members). The vertical tapering will thus need to be revised.

The adaptive hybrid coefficients method is slightly more expensive than the standard hybrid as it requires additional computation related to the estimation of the hybrid coefficient at each assimilation step. Here, the hybridization coefficients are estimated at every 5 grid cells, but we could have estimated them at every 10 grid cells (reducing the cost by 4) with a comparable solution (not shown). Furthermore, as these coefficients converge rapidly to stable estimates (within 3 model years, showing only a weak seasonal variability). They could be stored and directly used instead of being recalculated every time. As such, we do not consider that the additional computational cost would be much larger than the standard hybrid, which also has an additional cost (empirical estimation of the global coefficient).

In this study, the estimation of the hybridization coefficients in the adaptive method is constant in the vertical. Nonetheless, adapting the method to estimate different hybridization coefficients for different vertical levels or variables would be relatively trivial. Furthermore, we tested the method for the particular case of assimilation of SST objective analysis, where we update a single water column with a single observation, (*i.e.*, "strong localization"). For the assimilation of temperature/salinity profile data, the observation error is uncorrelated, and a larger localisation radius is used in NorCPM, the method can be adjusted following Ménérier (2021).

A critical assumption made with the adaptive hybrid covariance method is that models are unbiased and that for an infinite ensemble size, the ensemble covariance matrix converges with the true covariance matrix. These assumptions fall apart with Earth System Models with considerable biases (Palmer & Stevens, 2019). It remains to be verified how the method would perform in a real framework. Verification of the method in a real framework, both for coupled reanalysis and testing the impact on prediction initialised from it, will be tested in the future.

## Appendix A Minimization of the function $e$

The function  $e$  is defined as:

$$e(\alpha_d, \alpha_s) = \mathbb{E} \left[ \|\alpha_d \mathbf{P}_d + \alpha_s \mathbf{P}_s - \mathbf{P}\|^2 \right]. \quad (\text{A1})$$

By linearity of the expectation operator and by definition of the  $L_2$ -norm  $\|\cdot\|$ , we can write:

$$e(\alpha_d, \alpha_s) = \alpha_d^2 \mathbb{E} \left[ \|\mathbf{P}_d\|^2 \right] + \alpha_s \|\mathbf{P}_s\|^2 + \mathbb{E} \left[ \|\mathbf{P}\|^2 \right] + 2\alpha_d \alpha_s \mathbb{E} [\mathbf{P}_d \cdot \mathbf{P}_s] - 2\alpha_d \mathbb{E} [\mathbf{P}_d \cdot \mathbf{P}] - 2\alpha_s \mathbb{E} [\mathbf{P} \cdot \mathbf{P}_s]. \quad (\text{A2})$$

It follows from Eq. (15b) that:

$$\mathbb{E} [\mathbf{P}_d \cdot \mathbf{P}] = \mathbb{E} \left[ \|\mathbf{P}\|^2 \right] \quad (\text{A3})$$

Replacing Eq. (A3) in Eq. (A2), we obtain the following expression of  $e$ :

$$e(\alpha_d, \alpha_s) = \alpha_d^2 \mathbb{E} \left[ \|\mathbf{P}_d\|^2 \right] + \alpha_s^2 \|\mathbf{P}_s\|^2 + (1 - 2\alpha_d) \mathbb{E} \left[ \|\mathbf{P}\|^2 \right] + 2\alpha_s(\alpha_d - 1) \mathbb{E} [\mathbf{P}_d \cdot \mathbf{P}_s]. \quad (\text{A4})$$

$e$  being a quadratic function of two variables,  $\alpha_d$  and  $\alpha_s$ , with positive coefficients associated to  $\alpha_d^2$  and  $\alpha_s^2$ , its has a unique minimum where both the partial derivatives with respect to  $\alpha_d$  and  $\alpha_s$  are null. Hence, minimizing the function  $e$  is equivalent to solve the following system of two equations:

$$\begin{cases} \frac{\partial e(\alpha_d, \alpha_s)}{\partial \alpha_d} = 0 \\ \frac{\partial e(\alpha_d, \alpha_s)}{\partial \alpha_s} = 0 \end{cases} \quad (\text{A5})$$

The partial derivatives of  $e$  with respect to  $\alpha_d$  and  $\alpha_s$  are given by Eq. (A6) and (A7):

$$\frac{\partial e(\alpha_d, \alpha_s)}{\partial \alpha_d} = 2\alpha_d \mathbb{E} \left[ \|\mathbf{P}_d\|^2 \right] + 2\alpha_s \mathbb{E} [\mathbf{P}_s \cdot \mathbf{P}_d] - 2\mathbb{E} \left[ \|\mathbf{P}\|^2 \right], \quad (\text{A6})$$

$$\frac{\partial e(\alpha_d, \alpha_s)}{\partial \alpha_s} = 2\alpha_d \mathbb{E} [\mathbf{P}_s \cdot \mathbf{P}_d] + 2\alpha_s \|\mathbf{P}_s\|^2 - 2\mathbb{E} [\mathbf{P}_s \cdot \mathbf{P}_d]. \quad (\text{A7})$$

From which it follows that minimizing the function  $e$  is equivalent to solving the system of two equations:

$$\begin{cases} \alpha_d \mathbb{E} \left[ \|\mathbf{P}_d\|^2 \right] + \alpha_s \mathbb{E} [\mathbf{P}_d \cdot \mathbf{P}_s] = \mathbb{E} \left[ \|\mathbf{P}\|^2 \right] \\ \alpha_d \mathbb{E} [\mathbf{P}_d \cdot \mathbf{P}_s] + \alpha_s \|\mathbf{P}_s\|^2 = \mathbb{E} [\mathbf{P}_d \cdot \mathbf{P}_s], \end{cases} \quad (\text{A8})$$

## Appendix B Benefits of hybridization

By definition of the function  $e$ :

$$e(1, 0) = \mathbb{E} \left[ \|\mathbf{P}_d - \mathbf{P}\|^2 \right]. \quad (\text{B1})$$

562 By linearity of the expectation operator and by definition of the  $L_2$ -norm, we can  
563 show that

$$564 \quad e(1, 0) = \mathbb{E} \left[ \|\mathbf{P}_d\|^2 \right] + \mathbb{E} \left[ \|\mathbf{P}\|^2 \right] - 2\mathbb{E} [\mathbf{P}_d \cdot \mathbf{P}]. \quad (\text{B2})$$

565 Replacing Eq. (A3) in Eq. (B2) we get:

$$566 \quad e(1, 0) = \mathbb{E} \left[ \|\mathbf{P}_d\|^2 \right] - \mathbb{E} \left[ \|\mathbf{P}\|^2 \right] \quad (\text{B3})$$

567 From which we can express the difference of the errors between the EnKF and the  
568 hybrid scheme:

$$569 \quad e(1, 0) - e(\alpha_d, \alpha_s) = (1 - \alpha_d^2)\mathbb{E} \left[ \|\mathbf{P}_d\|^2 \right] - 2(1 - \alpha_d)\mathbb{E} \left[ \|\mathbf{P}\|^2 \right] - \alpha_s^2 \|\mathbf{P}_s\|^2 - 2\alpha_s(\alpha_d - 1)\mathbb{E} [\mathbf{P}_s \cdot \mathbf{P}_d]. \quad (\text{B4})$$

571 For the sake of simplicity, we note:

$$572 \quad \alpha = \mathbb{E} \left[ \|\mathbf{P}\|^2 \right], \quad (\text{B5})$$

$$573 \quad \beta = \|\mathbf{P}_s\|^2, \quad (\text{B6})$$

$$574 \quad \gamma = \mathbb{E} [\mathbf{P}_d \cdot \mathbf{P}_s], \quad (\text{B7})$$

$$575 \quad \delta = \mathbb{E} \left[ \|\mathbf{P}_d\|^2 \right]. \quad (\text{B8})$$

576 Eq. (B4) rewrites:

$$577 \quad e(1, 0) - e(\alpha_d, \alpha_s) = (1 - \alpha_d^2)\delta - 2(1 - \alpha_d)\alpha - \alpha_s^2\beta - 2\alpha_s(\alpha_d - 1)\gamma. \quad (\text{B9})$$

578 Given that  $\alpha_d = \frac{n_d}{\Delta}$  and  $\alpha_s = \frac{n_s}{\Delta}$ :

$$579 \quad e(1, 0) - e(\alpha_d, \alpha_s) = \frac{(\Delta^2 - n_d^2)\delta - 2(\Delta^2 - \Delta n_d)\alpha - n_s^2\beta - 2n_s(n_d - \Delta)\gamma}{\Delta^2}. \quad (\text{B10})$$

580  $\Delta^2$  being positive, showing that  $e(1, 0) - e(\alpha_d, \alpha_s) \geq 0$  is equivalent to show that:

$$581 \quad (\Delta^2 - n_d^2)\delta - 2(\Delta^2 - \Delta n_d)\alpha - n_s^2\beta - 2n_s(n_d - \Delta)\gamma \geq 0. \quad (\text{B11})$$

582 On the other hand,  $n_d$ ,  $n_s$ , and  $\Delta$  write:

$$583 \quad n_d = \alpha\beta - \gamma^2, \quad (\text{B12})$$

$$584 \quad n_s = \gamma\delta - \alpha\gamma, \quad (\text{B13})$$

$$585 \quad \Delta = \beta\delta - \gamma^2. \quad (\text{B14})$$

586 Replacing  $n_d$ ,  $n_s$ , and  $\Delta$  by their expression given by Eqs. (B12), (B13), and (B14)  
587 in the left hand side of Eq. (B11), and developing all the terms we can show that Eq. (B11)  
588 is verified if and only if:

$$\beta(\beta\delta - \gamma^2)(\delta - \alpha)^2 \geq 0. \quad (\text{B15})$$

590  $\beta \geq 0$  as a sum of squares and  $(\delta - \alpha)^2 \geq 0$  as a square. Showing that  $e(1, 0) -$   
 591  $e(\alpha_d, \alpha_s) \geq 0$  is then equivalent to show that  $\beta\delta \geq \gamma^2$  i-e  $\|\mathbf{P}_s\|^2 \mathbb{E} [\|\mathbf{P}_d\|^2] - \mathbb{E} [\mathbf{P}_d \cdot \mathbf{P}_s]^2 \geq$   
 592  $0$ . This inequality holds, see Appendix C, Eq. (C10), and replacing  $\mathbf{P}$  by  $\mathbf{P}_d$ . As a con-  
 593 sequence,  $e(1, 0) \geq e(\alpha_d, \alpha_s)$ .

### 594 Appendix C Collinearity/orthogonality of $\mathbb{E} [\mathbf{P}]$ and $\mathbf{P}_s$

595 We write  $\mathbf{P}_d$  as  $\mathbf{P}$  plus some error  $\varepsilon$ , and we assume that the static covariance  $\mathbf{P}_s$   
 596 is independent from that error, i-e:  $\mathbb{E} [\mathbf{P}_s \cdot \varepsilon] = 0$ . Therefore:

$$597 \quad \mathbb{E} [\mathbf{P}_d \cdot \mathbf{P}_s] = \mathbb{E} [\mathbf{P} \cdot \mathbf{P}_s + \mathbf{P}_s \cdot \varepsilon] = \mathbb{E} [\mathbf{P} \cdot \mathbf{P}_s] + \mathbb{E} [\mathbf{P}_s \cdot \varepsilon] = \mathbb{E} [\mathbf{P} \cdot \mathbf{P}_s]. \quad (\text{C1})$$

598 Thus, if  $\mathbb{E} [\mathbf{P}_d \cdot \mathbf{P}_s] = 0$  then  $\mathbb{E} [\mathbf{P} \cdot \mathbf{P}_s] = 0$  and  $\mathbf{P}$  and  $\mathbf{P}_s$  are orthogonal in a sta-  
 599 tistical sense.

600 Following Eq. (C1), we have:

$$601 \quad \|\mathbf{P}_s\|^2 \mathbb{E} [\|\mathbf{P}\|^2] - \mathbb{E} [\mathbf{P}_d \cdot \mathbf{P}_s]^2 = \|\mathbf{P}_s\|^2 \mathbb{E} [\|\mathbf{P}\|^2] - \mathbb{E} [\mathbf{P} \cdot \mathbf{P}_s]^2. \quad (\text{C2})$$

602 By definition of  $\|\mathbf{P}_s\|^2$  and  $\mathbb{E} [\|\mathbf{P}\|^2]$ :

$$603 \quad \|\mathbf{P}_s\|^2 \mathbb{E} [\|\mathbf{P}\|^2] = \sum_{i=1}^p \mathbf{P}_{si}^2 \mathbb{E} [\mathbf{P}_i^2] + \sum_{1 \leq i \neq j \leq p} \mathbf{P}_{si}^2 \mathbb{E} [\mathbf{P}_j^2], \quad (\text{C3})$$

$$604 \quad \|\mathbf{P}_s\|^2 \mathbb{E} [\|\mathbf{P}\|^2] = \sum_{i=1}^p \mathbf{P}_{si}^2 (\text{Var}(\mathbf{P}_i) + \mathbb{E} [\mathbf{P}_i]^2) \\ 605 \quad + \sum_{1 \leq i \neq j \leq p} \mathbf{P}_{si}^2 (\text{Var}(\mathbf{P}_j) + \mathbb{E} [\mathbf{P}_j]^2), \quad (\text{C4})$$

$$606 \quad \|\mathbf{P}_s\|^2 \mathbb{E} [\|\mathbf{P}\|^2] = \sum_{i=1}^p \mathbf{P}_{si}^2 \mathbb{E} [\mathbf{P}_i]^2 + \sum_{1 \leq i \neq j \leq p} \mathbf{P}_{si}^2 \mathbb{E} [\mathbf{P}_j]^2 + \sum_{i=1}^p \mathbf{P}_{si}^2 \text{Var}(\mathbf{P}_i) \\ 607 \quad + \sum_{1 \leq i \neq j \leq p} \mathbf{P}_{si}^2 \text{Var}(\mathbf{P}_j). \quad (\text{C5})$$

608 On the other hand:

$$609 \quad \mathbb{E} [\mathbf{P} \cdot \mathbf{P}_s]^2 = \sum_{i=1}^p \mathbf{P}_{si}^2 \mathbb{E} [\mathbf{P}_i]^2 + 2 \sum_{1 \leq i < j \leq p} \mathbf{P}_{si} \mathbb{E} [\mathbf{P}_i] \mathbf{P}_{sj} \mathbb{E} [\mathbf{P}_j]. \quad (\text{C6})$$

610 Therefore:

$$\begin{aligned}
 611 \quad \|\mathbf{P}_s\|^2 \mathbb{E} [\|\mathbf{P}\|^2] - \mathbb{E} [\mathbf{P} \cdot \mathbf{P}_s]^2 &= \sum_{i=1}^p \mathbf{P}_{si}^2 \text{Var}(\mathbf{P}_i) + \sum_{1 \leq i \neq j \leq p} \mathbf{P}_{si}^2 \text{Var}(\mathbf{P}_j) \\
 612 &+ \sum_{1 \leq i \neq j \leq p} \mathbf{P}_{si}^2 \mathbb{E} [\mathbf{P}_j]^2 \\
 613 &- 2 \sum_{1 \leq i < j \leq p} \mathbf{P}_{si} \mathbb{E} [\mathbf{P}_i] \mathbf{P}_{sj} \mathbb{E} [\mathbf{P}_j], \quad (C7)
 \end{aligned}$$

$$\begin{aligned}
 614 \quad \|\mathbf{P}_s\|^2 \mathbb{E} [\|\mathbf{P}\|^2] - \mathbb{E} [\mathbf{P} \cdot \mathbf{P}_s]^2 &= \sum_{i=1}^p \mathbf{P}_{si}^2 \text{Var}(\mathbf{P}_i) + \sum_{1 \leq i \neq j \leq p} \mathbf{P}_{si}^2 \text{Var}(\mathbf{P}_j) \\
 615 &+ \sum_{1 \leq i < j \leq p} \mathbf{P}_{si}^2 \mathbb{E} [\mathbf{P}_j]^2 + \mathbf{P}_{sj}^2 \mathbb{E} [\mathbf{P}_i]^2 \\
 616 &- 2 \sum_{1 \leq i < j \leq p} \mathbf{P}_{si} \mathbb{E} [\mathbf{P}_i] \mathbf{P}_{sj} \mathbb{E} [\mathbf{P}_j], \quad (C8)
 \end{aligned}$$

$$\begin{aligned}
 617 \quad \|\mathbf{P}_s\|^2 \mathbb{E} [\|\mathbf{P}\|^2] - \mathbb{E} [\mathbf{P} \cdot \mathbf{P}_s]^2 &= \sum_{i=1}^p \mathbf{P}_{si}^2 \text{Var}(\mathbf{P}_i) + \sum_{1 \leq i \neq j \leq p} \mathbf{P}_{si}^2 \text{Var}(\mathbf{P}_j) \\
 618 &+ \sum_{1 \leq i < j \leq p} (\mathbf{P}_{si} \mathbb{E} [\mathbf{P}_j] - \mathbf{P}_{sj} \mathbb{E} [\mathbf{P}_i])^2 \quad (C9)
 \end{aligned}$$

619 As a consequence,

$$620 \quad \|\mathbf{P}_s\|^2 \mathbb{E} [\|\mathbf{P}\|^2] - \mathbb{E} [\mathbf{P} \cdot \mathbf{P}_s]^2 \geq 0, \quad (C10)$$

621 as the sum of positive terms, and  $\|\mathbf{P}_s\|^2 \mathbb{E} [\|\mathbf{P}\|^2] - \mathbb{E} [\mathbf{P} \cdot \mathbf{P}_s]^2$  is equal to 0 if and only  
 622 if  $\text{Var}(\mathbf{P}_i) = 0$  for all  $i = 1, \dots, p$  and  $(\mathbf{P}_{si} \mathbb{E} [\mathbf{P}_j] - \mathbf{P}_{sj} \mathbb{E} [\mathbf{P}_i])^2 = 0$  for all  $1 \leq i < j \leq$   
 623  $p$ . In particular, this condition is equivalent to:

$$624 \quad \mathbf{P}_{s1} \mathbb{E} [\mathbf{P}_j] = \mathbf{P}_{sj} \mathbb{E} [\mathbf{P}_1], \quad j = 2, \dots, p, \quad (C11)$$

625 which means that  $\mathbf{P}_s$  and  $\mathbb{E} [\mathbf{P}]$  are collinear.

## 626 Open Research

627 All the data used to make this study are available from: <https://zenodo.org/record/8037714>  
 628 (DOI: 10.5281/zenodo.8037714)

629 The figures were made using:

- 630 • Matlab version 2021-b available from: <https://se.mathworks.com/products/matlab.html>
- 631 • matplotlib version 3.5.2 available from: <https://matplotlib.org/>

## 632 Acknowledgments

633 This study was supported by Horizon Europe (#101081555), the Research Council of  
 634 Norway (Grant No. 301396) the Trond Mohn Foundation under project number: BFS2018TMT01.  
 635 This work has also received a grant for computer time from the Norwegian Program for  
 636 supercomputing (NOTUR2, project number NN9039K) and a storage Grant (NORSTORE,  
 637 NS9039K).

## References

- Anderson, J. L. (2001). An ensemble adjustment Kalman filter for data assimilation. *Monthly Weather Review*, *129*(12), 2884–2903. doi: 10.1175/1520-0493(2001)129<2884:AEAKFF>2.0.CO;2
- Anderson, J. L. (2007). Exploring the need for localization in ensemble data assimilation using a hierarchical ensemble filter. *Physica D: Nonlinear Phenomena*, *230*(1-2), 99–111. doi: 10.1016/j.physd.2006.02.011
- Bauer, H.-s., Schwitalla, T., Wulfmeyer, V., Bakhshaii, A., Ehret, U., Neuper, M., & Caumont, O. (2015). Quantitative precipitation estimation based on high-resolution numerical weather prediction and data assimilation with WRF – a performance test. *Tellus, Series A: Dynamic Meteorology and Oceanography*, *0870*(67), 25047. doi: 10.3402/tellusa.v67.25047
- Bentsen, M., Bethke, I., Debernard, J. B., Iversen, T., Kirkevåg, A., Seland, Ø., ... Kristjánsson, J. E. (2013). The Norwegian Earth System Model, NorESM1-M – Part 1: Description and basic evaluation of the physical climate. *Geoscientific Model Development*, *6*(3), 687–720. doi: 10.5194/gmd-6-687-2013
- Bethke, I., Wang, Y., Counillon, F., Keenlyside, N., Kimmritz, M., Fransner, F., ... Eldevik, T. (2021). NorCPM1 and its contribution to CMIP6 DCPP. *Geoscientific Model Development*, *14*(11), 7073–7116. doi: 10.5194/gmd-14-7073-2021
- Bethke, I., Wang, Y., Counillon, F., Kimmritz, M., Langehaug, H., Bentsen, M., & Keenlyside, N. (2018). Subtropical north atlantic preconditioning key to skillful subpolar gyre prediction.
- Bishop, C. H., & Hodyss, D. (2007). Flow-adaptive moderation of spurious ensemble correlations and its use in ensemble-based data assimilation. *Quarterly Journal of the Royal Meteorological Society*, *133*, 2029–2044.
- Bitz, C. M., Shell, K. M., Gent, P. R., Bailey, D. A., Danabasoglu, G., Armour, K. C., ... Kiehl, J. T. (2012). Climate sensitivity of the community climate system model, version 4. *Journal of Climate*, *25*(9), 3053–3070. doi: 10.1175/JCLI-D-11-00290.1
- Boer, G. J., Smith, D. M., Cassou, C., Doblas-Reyes, F., Danabasoglu, G., Kirtman, B., ... others (2016). The decadal climate prediction project (dcpp) contribution to cmip6. *Geoscientific Model Development*, *9*(10), 3751–3777.
- Brune, S., Nerger, L., & Baehr, J. (2015). Assimilation of oceanic observations in a global coupled earth system model with the seik filter. *Ocean Modelling*, *96*, 254–264.
- Cardinali, C., Pezzulli, S., & Andersson, E. (2004). Influence-matrix diagnostic of a data assimilation system. *Quarterly Journal of the Royal Meteorological Society: A journal of the atmospheric sciences, applied meteorology and physical oceanography*, *130*(603), 2767–2786.
- Carrassi, A., Bocquet, M., Bertino, L., & Evensen, G. (2018). Data assimilation in the geosciences: An overview of methods, issues, and perspectives. *Wiley Interdisciplinary Reviews: Climate Change*, *9*(5), 1–50. doi: 10.1002/wcc.535
- Carrió, D. S., Bishop, C. H., & Kotsuki, S. (2021). Empirical determination of the covariance of forecast errors: An empirical justification and reformulation of hybrid covariance models. *Quarterly Journal of the Royal Meteorological Society*, *147*(736), 2033–2052. doi: 10.1002/qj.4008
- Counillon, F., & Bertino, L. (2009). Ensemble optimal interpolation: multivariate properties in the gulf of mexico. *Tellus A: Dynamic Meteorology and Oceanography*, *61*(2), 296–308.
- Counillon, F., Bethke, I., Keenlyside, N., Bentsen, M., Bertino, L., & Zheng, F. (2014). Seasonal-to-decadal predictions with the ensemble kalman filter and the Norwegian earth System Model: A twin experiment. *Tellus, Series A: Dynamic Meteorology and Oceanography*, *66*(1). doi: 10.3402/tellusa.v66.21074
- Counillon, F., Keenlyside, N., Bethke, I., Wang, Y., Billeau, S., Shen, M. L., &

- 693 Bentsen, M. (2016). Flow-dependent assimilation of sea surface tem-  
 694 perature in isopycnal coordinates with the Norwegian Climate Prediction  
 695 Model. *Tellus, Series A: Dynamic Meteorology and Oceanography*, *68*(1). doi:  
 696 10.3402/tellusa.v68.32437
- 697 Counillon, F., Keenlyside, N., Toniazzo, T., Koseki, S., Demissie, T., Bethke, I., &  
 698 Wang, Y. (2021). Relating model bias and prediction skill in the equatorial  
 699 atlantic. *Climate Dynamics*, *56*, 2617–2630.
- 700 Counillon, F., Sakov, P., & Bertino, L. (2009). Application of a hybrid EnKF-OI to  
 701 ocean forecasting. *Ocean Science*, *5*(4), 389–401. doi: 10.5194/os-5-389-2009
- 702 Craig, A. P., Vertenstein, M., & Jacob, R. (2012). A new flexible coupler for  
 703 earth system modeling developed for CCSM4 and CESM1. *International*  
 704 *Journal of High Performance Computing Applications*, *26*(1), 31–42. doi:  
 705 10.1177/1094342011428141
- 706 Evensen, G. (2003). The Ensemble Kalman Filter: Theoretical formulation and  
 707 practical implementation. *Ocean Dynamics*, *53*(4), 343–367. doi: 10.1007/  
 708 s10236-003-0036-9
- 709 Frankcombe, L. M., McGregor, S., & England, M. H. (2015). Robustness of the  
 710 modes of indo-pacific sea level variability. *Climate dynamics*, *45*, 1281–1298.
- 711 Gharamti, M. E. (2020). Hybrid ensemble-variational filter: A spatially and tem-  
 712 porally varying adaptive algorithm to estimate relative weighting. *Monthly*  
 713 *Weather Review*, *149*(1), 65–76. doi: 10.1175/MWR-D-20-0101.1
- 714 Gharamti, M. E., Valstar, J., & Hoteit, I. (2014). An adaptive hybrid EnKF-  
 715 OI scheme for efficient state-parameter estimation of reactive contaminant  
 716 transport models. *Advances in Water Resources*, *71*, 1–15. Retrieved  
 717 from <http://dx.doi.org/10.1016/j.advwatres.2014.05.001> doi:  
 718 10.1016/j.advwatres.2014.05.001
- 719 Guemas, V., Corti, S., García-Serrano, J., Doblas-Reyes, F., Balmaseda, M., & Mag-  
 720 nusson, L. (2013). The indian ocean: The region of highest skill worldwide in  
 721 decadal climate prediction. *Journal of Climate*, *26*(3), 726–739.
- 722 Hamill, T. M., & Snyder, C. (2000). A Hybrid Ensemble Kalman Filter–3D  
 723 Variational Analysis Scheme. *Monthly Weather Review*, *128*(8), 2905–  
 724 2919. Retrieved from [http://journals.ametsoc.org/doi/abs/10.1175/  
 725 1520-0493%282000%29128%3C2905%3AAHEKfV%3E2.0.CO%3B2](http://journals.ametsoc.org/doi/abs/10.1175/1520-0493%282000%29128%3C2905%3AAHEKfV%3E2.0.CO%3B2) doi: 10.1175/  
 726 1520-0493(2000)128(2905:AHEKfV)2.0.CO;2
- 727 Houtekamer, P. L., & Mitchell, H. L. (2001). A Sequential Ensemble Kalman Filter  
 728 for Atmospheric Data Assimilation. *Monthly Weather Review*, *129*, 123–137.
- 729 Hurrell, J. W., Holland, M. M., Gent, P. R., Ghan, S., Kay, J. E., Kushner, P. J.,  
 730 ... Marshal, S. (2013). The community earth system model: a framework for  
 731 collaborative research. *American Meteorological Society*(September), 1339–  
 732 1360. doi: 10.1175/BAMS-D-12-00121.1
- 733 Karspeck, A. R., Danabasoglu, G., Anderson, J., Karol, S., Collins, N., Vertenstein,  
 734 M., ... others (2018). A global coupled ensemble data assimilation system  
 735 using the community earth system model and the data assimilation research  
 736 testbed. *Quarterly Journal of the Royal Meteorological Society*, *144*(717),  
 737 2404–2430.
- 738 Lawrence, D. M., Oleson, K. W., Flanner, M. G., Thornton, P. E., Swenson, S. C.,  
 739 Lawrence, P. J., ... Slater, A. G. (2011). Parameterization improvements  
 740 and functional and structural advances in Version 4 of the Community Land  
 741 Model. *Journal of Advances in Modeling Earth Systems*, *3*, 1–27. doi:  
 742 10.1029/2011ms000045
- 743 Ménétrier, B. (2021). *Sample covariance filtering* (Tech. Rep.). Retrieved from  
 744 [https://github.com/benjaminmenetrier/covariance\\_filtering/blob/  
 745 8b2fa7366943cff8de40fa858e0a0a153b63eb90/covariance\\_filtering.pdf](https://github.com/benjaminmenetrier/covariance_filtering/blob/8b2fa7366943cff8de40fa858e0a0a153b63eb90/covariance_filtering.pdf)
- 746 Ménétrier, B., & Auligné, T. (2015). Optimized Localization and Hybridization to  
 747 Filter Ensemble-Based Covariances. *Monthly Weather Review*, *143*(10), 3931–

3947. doi: 10.1175/mwr-d-15-0057.1
- 748  
749 Ménétrier, B., Montmerle, T., Michel, Y., & Berre, L. (2015). Linear Filtering  
750 of Sample Covariances for Ensemble-Based Data Assimilation. Part I: Op-  
751 timality Criteria and Application to Variance Filtering and Covariance Lo-  
752 calization. *Monthly Weather Review*, *143*(5), 1622–1643. Retrieved from  
753 <http://journals.ametsoc.org/doi/10.1175/MWR-D-14-00157.1> doi:  
754 10.1175/MWR-D-14-00157.1
- 755 Oke, P. R., Brassington, G. B., Griffin, D. A., & Schiller, A. (2008). The bluelink  
756 ocean data assimilation system (bodas). *Ocean modelling*, *21*(1-2), 46–70.
- 757 Oke, P. R., Sakov, P., & Corney, S. P. (2007). Impacts of localisation in the EnKF  
758 and EnOI: Experiments with a small model. *Ocean Dynamics*, *57*(1), 32–45.  
759 doi: 10.1007/s10236-006-0088-8
- 760 Ott, E., Hunt, B. R., Szunyogh, I., Zimin, A. V., Kostelich, E. J., Corazza, M., ...  
761 Yorke, J. A. (2004). A local ensemble Kalman filter for atmospheric data as-  
762 similation. *Tellus A: Dynamic Meteorology and Oceanography*, *56*(5), 415–428.  
763 doi: 10.3402/tellusa.v56i5.14462
- 764 O’Kane, T. J., Sandery, P. A., Monselesan, D. P., Sakov, P., Chamberlain, M. A.,  
765 Matear, R. J., ... Stevens, L. (2019). Coupled data assimilation and ensem-  
766 ble initialization with application to multiyear enso prediction. *Journal of*  
767 *Climate*, *32*(4), 997–1024.
- 768 Palmer, T., & Stevens, B. (2019). The scientific challenge of understanding and  
769 estimating climate change. *Proceedings of the National Academy of Sciences*,  
770 *116*(49), 24390–24395.
- 771 Raanes, P. N., Bocquet, M., & Carrassi, A. (2019). Adaptive covariance inflation  
772 in the ensemble Kalman filter by Gaussian scale mixtures. *Quarterly Journal*  
773 *of the Royal Meteorological Society*, *145*(January 2018), 53–75. doi: 10.1002/qj  
774 .3386
- 775 Raboudi, N. F., Ait-El-Fquih, B., Dawson, C., & Hoteit, I. (2019). Combining Hy-  
776 brid and One-Step-Ahead Smoothing for Efficient Short-Range Storm Surge  
777 Forecasting with an Ensemble Kalman Filter. *Monthly Weather Review*, 3283–  
778 3300. doi: 10.1175/MWR-D-18-0410.1
- 779 Rainwater, S., & Hunt, B. (2013). Mixed-Resolution Ensemble Data Assimilation.  
780 *Monthly Weather Review*, *141*(9), 3007–3021. doi: 10.1175/mwr-d-12-00234.1
- 781 Sakov, P., Counillon, F., Bertino, L., Lister, K. A., Oke, P. R., & Korabely, A.  
782 (2012). TOPAZ4: An ocean-sea ice data assimilation system for the North At-  
783 lantic and Arctic. *Ocean Science*, *8*(4), 633–656. doi: 10.5194/os-8-633-2012
- 784 Sakov, P., Evensen, G., & Bertino, L. (2010). Asynchronous data assimilation with  
785 the enfk. *Tellus A: Dynamic Meteorology and Oceanography*, *62*(1), 24–29.
- 786 Sakov, P., & Oke, P. R. (2008). A deterministic formulation of the ensemble  
787 Kalman filter: An alternative to ensemble square root filters. *Tellus, Se-*  
788 *ries A: Dynamic Meteorology and Oceanography*, *60 A*(2), 361–371. doi:  
789 10.1111/j.1600-0870.2007.00299.x
- 790 Taylor, K. E., Stouffer, R. J., & Meehl, G. A. (2012). An overview of CMIP5 and  
791 the experiment design. *Bulletin of the American Meteorological Society*, *93*(4),  
792 485–498. doi: 10.1175/BAMS-D-11-00094.1
- 793 van Vuuren, D. P., Edmonds, J., Kainuma, M., Riahi, K., Thomson, A., Hibbard,  
794 K., ... Rose, S. K. (2011). The representative concentration pathways: An  
795 overview. *Climatic Change*, *109*(1), 5–31. doi: 10.1007/s10584-011-0148-z
- 796 Wahba, G., Johnson, D. R., Gao, F., & Gong, J. (1995). Adaptive tuning of numeri-  
797 cal weather prediction models: Randomized gcv in three-and four-dimensional  
798 data assimilation. *Monthly Weather Review*, *123*(11), 3358–3370.
- 799 Wang, X., Hamill, T. M., Whitaker, J. S., & Bishop, C. H. (2007). A Comparison  
800 of Hybrid Ensemble Transform Kalman Filter – Optimum Interpolation and  
801 Ensemble Square Root Filter Analysis Schemes. *Monthly Weather Review*,  
802 1055–1076. doi: 10.1175/MWR3307.1

- 803 Wang, Y., Counillon, F., Barthélémy, S., & Barth, A. (2022). Benefit of vertical  
 804 localization for sea surface temperature assimilation in isopycnal coordinate  
 805 model. *Frontiers in Climate*, 4.
- 806 Wang, Y., Counillon, F., & Bertino, L. (2016). Alleviating the bias induced by the  
 807 linear analysis update with an isopycnal ocean model. *Quarterly Journal of the*  
 808 *Royal Meteorological Society*, 142(695), 1064–1074.
- 809 Weaver, A., & Courtier, P. (2001). Generalized Diffusion. *Quarterly Journal of the*  
 810 *Royal Meteorological Society*, 127, 1815–1846.
- 811 Whitaker, J. S., & Hamill, T. M. (2012). Evaluating Methods to Account for Sys-  
 812 tem Errors in Ensemble Data Assimilation. *Monthly Weather Review*, 140(9),  
 813 3078–3089. doi: 10.1175/mwr-d-11-00276.1
- 814 Xie, J., Counillon, F., & Bertino, L. (2018). Impact of assimilating a merged sea-  
 815 ice thickness from cryosat-2 and smos in the arctic reanalysis. *The Cryosphere*,  
 816 12(11), 3671–3691.
- 817 Zhang, S., Rosati, A., & Harrison, M. (2009). Detection of multidecadal oceanic  
 818 variability by ocean data assimilation in the context of a “perfect” coupled  
 819 model. *Journal of Geophysical Research: Oceans*, 114(C12).